A&A 482, 397–402 (2008)
DOI: 10.1051/0004-6361:20079252

Astronomy & Astrophysics

Non-thermal emission from secondary pairs in close TeV binary systems

V. Bosch-Ramon[1], D. Khangulyan[1], and F. A. Aharonian[2,1]

[1] Max Planck Institut für Kernphysik, Saupfercheckweg 1, Heidelberg 69117, Germany
e-mail: [vbosch;Dmitry.Khangulyan]@mpi-hd.mpg.de; Felix.Aharonian@dias.ie
[2] Dublin Institute for Advanced Studies, Dublin, Ireland

Received 14 December 2007 / Accepted 22 January 2008

ABSTRACT

Context. Massive hot stars produce dense ultraviolet (UV) photon fields in their surroundings. If a very high-energy (VHE) gamma ray emitter is located close to the star, then gamma rays are absorbed in the stellar photon field, creating secondary (electron-positron) pairs.
Aims. We study the broadband emission of these secondary pairs in the stellar photon and magnetic fields.
Methods. Under certain assumptions regarding the stellar wind and the magnetic field in the surroundings of a massive hot star, we calculate the steady state energy distribution of secondary pairs created in the system and its radiation from radio to gamma rays.
Results. Under the ambient magnetic field, possibly high enough to suppress electromagnetic (EM) cascading, the energy of secondary pairs is radiated via synchrotron and single IC scattering producing radio-to-gamma ray radiation. The synchrotron spectral energy distribution (SED) is hard, peaks around X-ray energies, and becomes softer. The IC SED is hard as well and peaks around 10 GeV, also becoming softer at higher energies due to synchrotron loss dominance.
Conclusions. The radio emission from secondary pairs is moderate and detectable as a point-like and/or extended source. In X-rays, the secondary pair synchrotron component may be dominant. At energies $\lesssim$10 GeV, the secondary pair IC radiation may be dominant over the primary gamma ray emission, and possibly detectable by the next generation of instruments.

Key words. gamma rays: theory – X-rays: binaries – radiation mechanisms: non-thermal – stars: individual: LS 5039

1. Introduction

Recently, several compact TeV emitters harboring an OB type star have been found in our Galaxy: PSR B1259−63 is a massive binary system containing a young non-accreting pulsar detected by HESS (Aharonian et al. 2005a); LS 5039 is likely a high-mass microquasar also detected by HESS (Aharonian et al. 2005b); LS I +61 303 is a high-mass X-ray binary detected first by MAGIC (Albert et al. 2006) and recently also by VERITAS (Maier 2007); Cygnus X-1 is a high-mass microquasar harboring a black hole detected by MAGIC (Albert et al. 2007). In this type of objects a significant fraction of the energy radiated above 100 GeV can be absorbed via photon-photon interactions (e.g. Ford 1984; Protheroe & Stanev 1987; Moskalenko & Karakula 1994, Bednarek 1997; Boettcher & Dermer 2005; Dubus 2006a; Khangulyan et al. 2008; Reynoso et al. 2008) producing secondary pairs that, under the strong radiation and magnetic fields present close to the massive star, can radiate efficiently via IC or synchrotron processes. In the case in which IC is the dominant cooling channel, EM cascades can develop (see, e.g., Aharonian et al. 2006a; Bednarek 2006; Khangulyan et al. 2008; Orellana et al. 2007). If synchrotron emission is the dominant cooling channel, the absorbed radiation is reemitted at lower energies (e.g. Khangulyan et al. 2008). We note that the scenario described here could take place not only in microquasars or non-accreting pulsar systems but in any source harboring a gamma ray emitter embedded in a dense photon field.

In this work, we study the radiation of the secondary pairs created by photon-photon absorption of gamma rays in the surroundings of a hot massive star. We focus mainly on the case when the ambient magnetic field is strong enough to effectively suppress EM cascading. The structure of the paper is as follows: in Sect. 2, the adopted model is described; in Sect. 3, the results are presented and discussed, and our conclusions are given in Sect. 4.

2. A model for pair creation and secondary pair emission

2.1. The general picture

We describe here the physical system formed by an OB star and a gamma ray emitter separated by a short distance. The star is approximated as a point-like source of (monoenergetic) photons of energy ϵ_0 and luminosity L_*. The emitter, located at distance $R = d_*$ from the star and assumed to be point-like, isotropically produces gamma rays with an injection power $L_{\gamma\,\mathrm{inj}}$, following a power law distribution of index Γ. We consider here only the primary radiation above the minimum threshold energy for secondary pair production, i.e. $\epsilon_{\mathrm{min\ th}} = 1/\epsilon_0$ (in $m_\mathrm{e}c^2$ units), since we focus on the study of the production of secondary pairs and their emission. The maximum energy of the primary photons is fixed at 100 TeV. Throughout most of this work, we characterize the star/VHE emitter as follows: $L_* = 10^{39}$ erg/s, $d_* = 3\times10^{12}$ cm s^{-1}, and $\epsilon_0 = 2\times10^{-5}$ (corresponding to a star temperature $\approx$40 000 k); we take two values for Γ, 2 and 3, to account either for hard or soft primary gamma ray spectra.

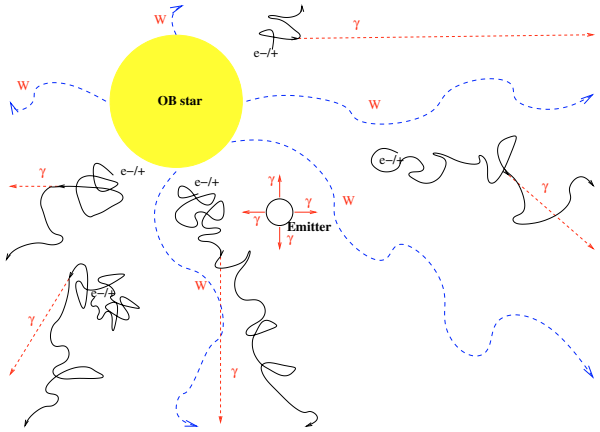

Fig. 1. Sketch of the physical scenario considered here. The long-dashed lines represent the wind, the straight dashed lines the secondary pair radiation, the straight solid lines the primary gamma rays, and the curved solid lines the advected/diffusing secondary pairs.

Important ingredients of the model are the stellar wind and the ambient magnetic field. OB stars present fast winds with mass loss rates $\dot{M}_{\rm w} \sim 10^{-7}$–$10^{-5}\ M_\odot\ {\rm yr}^{-1}$ and velocities $V_{\rm w} \sim (1$–$3) \times 10^8$ cm s^{-1} (e.g. Puls et al. 2006). We adopt here $\dot{M}_{\rm w} = 10^{-6}\ M_\odot\ {\rm yr}^{-1}$ and $V_{\rm w} = 2 \times 10^8$ cm s^{-1}. Moreover, the star generates a magnetic field in its surroundings with values on the stellar surface that might be as high as $B_0 \sim 1000$ G (e.g. Donati et al. 2002; Hubrig et al. 2007). We assume here that a significant fraction of the magnetic field is disordered. A sketch of our scenario is presented in Fig. 1.

2.2. Secondary pairs in the system

To compute the secondary pair injection spectra in the different regions of the binary system, we use the anisotropic differential pair production cross section given by Eq. (15) in Böttcher & Schlickeiser (1997). The secondary pair injection spectrum presents a slope similar to that of the primary gamma rays, with the low-energy cutoff similar to the pair creation one, which depends on the angle between the two incoming photons: $\sim\epsilon_{\rm th} = 2/[\epsilon_0(1-\cos\theta_{\gamma\gamma})]$. The point-like approximation for the star fails for $R \lesssim 2R_* \sim 20\,R_\odot$ from the stellar center. For our choice of values of d_*, R_*, L_*, and ϵ_0, only photons with energy >few TeV emitted at an angle $\lesssim$30° with respect to the star-emitter line can reach the region where the finite size of the star comes into play (Dubus 2006a). The monoenergetic photon target approximation is roughly valid provided we deal with a broad distribution of primary gamma rays. The deviation from the real case is small and will be neglected here.

We assume that diffusion in the wind takes place in the Bohm regime. Once secondary pairs are injected in different parts of the system, they isotropize and suffer wind advection, which is the dominant transport mechanism in the system. Ionization losses in the wind, synchrotron emission in the ambient magnetic field, and IC scattering of the stellar photons are the relevant cooling processes of secondary pairs ($\dot{\gamma}$). Relativistic Bremsstrahlung of the secondary pairs in the stellar wind is not considered since the timescales for this process are much longer than ionization, other radiative, and advective timescales. Adiabatic losses may play a role only at scales $\gg d_*$ and are not considered here. All dependencies on R of the relevant physical quantities (the wind density, and the energy densities of the ambient magnetic and stellar radiation fields) are taken as $\propto 1/R^2$. We consider that the TeV emitter produces radiation long enough for the formation of a steady state distribution of secondary pairs in the system ($n(\gamma, R)$), which can be obtained from the following differential equation:

$$V_{\rm w}\frac{\partial n(\gamma,R)}{\partial R} + \frac{\partial \dot{\gamma}(\gamma,R) n(\gamma,R)}{\partial \gamma} = q(\gamma,R), \quad (1)$$

where γ is the particle Lorentz factor and $q(\gamma, R)$ is the secondary pair injection rate as a function of energy and distance (derived in the appendix).

A restriction on $n(\gamma, R)$ is that EM cascades at 1 TeV must be effectively suppressed by the ambient B, which must therefore be above a certain critical value, $B_{\rm c}$ (see Khangulyan et al. 2008):

$$B_{\rm c} \approx 10\left(\frac{L_*}{10^{39}\ {\rm erg/s}}\right)^{1/2}\left(\frac{R}{R_*}\right)^{-1}\ {\rm G}. \quad (2)$$

Equation (2), together with the R-dependence assumed here, shows that EM cascades are already suppressed for a ≈3 G magnetic field at $R = d_*$. This value appears quite moderate when looking at the possible stellar surface magnetic field values given above. However, even in the case of weaker magnetic fields, $n(\gamma, R)$ does not change much if EM cascades are not accounted for $\Gamma \gtrsim 2.5$, since the amount of EM cascade reprocessed energy will be relatively small.

For the adopted parameter values in our model, most of the energy of the primary VHE radiation is absorbed for distances $\lesssim 10^{12}$ cm from the emitter and $\sim d_*$ from the star. Depending on Γ, radiative cooling leads to an electron distribution producing synchrotron emission that peaks either sharply at X-ray energies or smoothly in the range of X- to soft gamma rays. Along with this a fraction of the energy is radiated in the GeV range via IC scattering. The fact that the minimum energy of the injected secondary pairs is $\sim\epsilon_{\rm min\ th} m_{\rm e} c^2$ implies that, even under strong synchrotron or Thomson IC cooling, the emission of particles with energies below this value will not dominate the total radiative output. Ionization losses and wind advection lead to steady state secondary pairs radiating very little radio emission for $R \lesssim d_*$ from the star. However, the wind transports secondary pair energy to larger R, where this energy still can be efficiently radiated. In these farther regions, synchrotron radio emission can eventually become the dominant radiative channel.

3. Results

3.1. Injection and evolution of secondary pairs

In this section we discuss the spectrum of the secondary pairs injected in the system, $Q_{\rm int}(\gamma)(=\int q(\gamma,R){\rm d}R)$, and the secondary pair energy distribution once the steady state is reached, $N_{\rm int}(\gamma)(=\int n(\gamma,R){\rm d}R)$. For illustrative purposes, we perform our calculations using $L_{\gamma\ {\rm inj}} = 3 \times 10^{35}$ erg s^{-1}, which is similar to the value inferred in Khangulyan et al. (2008) for LS 5039. The secondary pair emission luminosity scales linearly with $L_{\gamma\ {\rm inj}}$.

In Figs. 2 and 3, upper panels, we show $Q_{\rm int}\,\gamma^2$ for the whole volume, adopting $\Gamma = 2$ and 3, respectively. In the same figures, lower panels, $N_{\rm int}\,\gamma^2$ for the whole region is also shown. In all the plots, the contributions to the total $Q_{\rm int}\,\gamma^2$ and $N_{\rm int}\,\gamma^2$ from $R < d_*$ and $>d_*$ are presented as well.

As seen in the figures, $Q_{\rm int}(\gamma)$ has a similar shape to that of the primary gamma rays $\propto\epsilon_\gamma^{-\Gamma}$. As mentioned in Sect. 2, the minimum energy of the injected secondary pairs is the pair creation

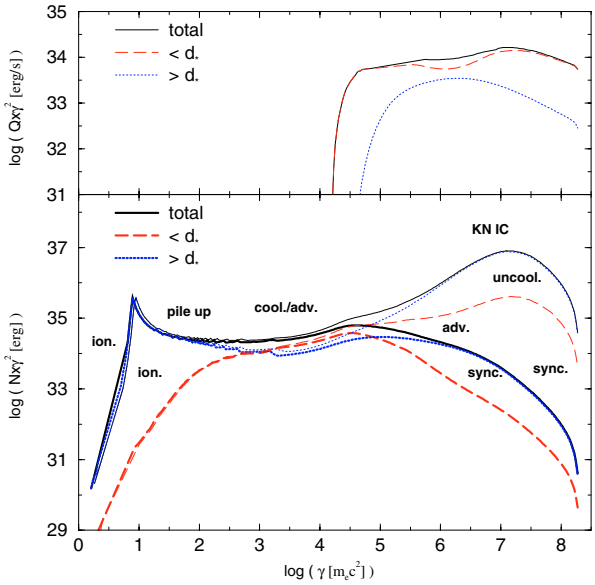

Fig. 2. *Upper panel*: total $Q_{\rm int}\,\gamma^2$ (solid line). $Q_{\rm int}\,\gamma^2$ for $R < d_*$ (long-dashed line) and $>d_*$ (dotted line) are also shown. We adopt $\Gamma = 2$. *Lower panel*: total $N_{\rm int}\,\gamma^2$ (solid line). $N_{\rm int}\,\gamma^2$ for $R < d_*$ (long-dashed line) and $>d_*$ (dotted line) are also shown. We adopt $\Gamma = 2$, and $B_0 = 1$ (thin lines) and 100 G (thick lines). The dominant cooling mechanisms at different energies are given.

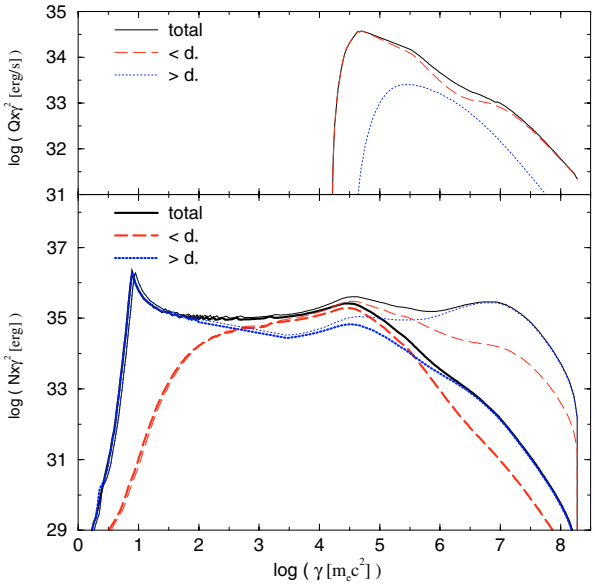

Fig. 3. The same as in Fig. 2 but for $\Gamma = 3$.

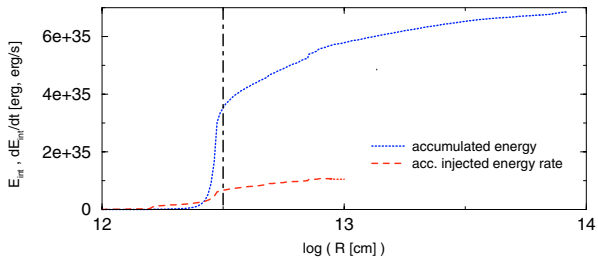

Fig. 4. The R-distribution of accumulated energy in secondary pairs (long-dashed line) and the R-distribution of accumulated energy rate via pair creation (dotted line) are shown. The location of the emitter is marked by a vertical thick dot-dashed line, at $\log(d_*)$. In the plot, the star location would be at the left.

threshold energy, i.e. $\epsilon_{\rm th} m_{\rm e} c^2$, which changes with the angle between the two incoming photons. As a consequence, both $q(\gamma, R)$ and $n(\gamma, R)$ depend strongly on R as well as on Γ. In addition, the shape of $N_{\rm int}(\gamma)$ is related to the dominance of different cooling mechanisms and the impact of wind advection.

For particle energies $>\epsilon_{\rm min\ th} m_{\rm e} c^2$, depending on γ, $N_{\rm int}(\gamma)$ is: cooled by synchrotron losses ($\propto\gamma^{-\Gamma-1}$; for high B in both $R < d_*$ and $>d_*$); uncooled (injection spectrum slope; for low B and $R < d_*$ because of the fast advection of the particles from this relatively small region) or cooled by KN IC ($\propto\gamma^{-\Gamma+1}$; mainly for low B and $R > d_*$ because there particles have time to lose energy). For particle energies $<\epsilon_{\rm min\ th} m_{\rm e} c^2$, $N_{\rm int}(\gamma)$ is: cooled by synchrotron/Thomson IC ($\propto\gamma^{-2}$; $R < d_*$); advection dominated ($\propto\gamma^{-2}$; $R > d_*$ because of advection of cooled particles created at $R < d_*$) or cooled by ionization losses ($\propto$constant; in both $R < d_*$ and $>d_*$). In the range $\gamma \sim 10$–100, the $1/R^2$-dependence of losses leads to a strong pileup of particles at $R \gg d_*$, giving a spike feature in the particle energy distribution. The cooling mechanisms in different γ ranges for $\Gamma = 2$ are indicated in Fig. 2, lower panel; for $\Gamma = 3$, despite the softer slope, the pattern is the same.

In Fig. 4, we present the total energy ($E_{\rm int}$ in Fig. 4) accumulated in secondary pairs up to distance R, and the total energy rate ($\mathrm{d}E_{\rm int}/\mathrm{d}t$ in Fig. 4) from pair creation accumulated up to R. The $\mathrm{d}E_{\rm int}/\mathrm{d}t$ curve is shown up to the distance at which injection becomes negligeable, i.e. $R_{\rm inj} \sim$ AU. As seen in Fig. 4, a significant amount of energy, $\sim 10^{35}$ erg, is transported up to several AU. Despite this energy budget, the efficiency of the emission from large R will be limited by the low magnetic and radiation energy densities and the ionization loss dominance.

3.2. Emission from secondary pairs

The calculated SEDs of the synchrotron and IC emission produced by the injected secondary pairs are shown in Figs. 5 and 6. In Fig. 5, we have adopted a $B = 100$ G, and $\Gamma = 2$ (upper panel) and 3 (lower panel). The SEDs of the emission generated at $R < d_*$ and $>d_*$ from the star are also shown. In Fig. 6, the SEDs have been computed adopting $B = 1$ (dotted line), 10 (long-dashed line) and 100 G (solid line), and $\Gamma = 2$ (upper panel) and 3 (lower panel).

For energies of photons produced by secondary pairs with energies $>\epsilon_{\rm min\ th} m_{\rm e} c^2$, the spectrum becomes softer for larger B due to the dominating synchrotron channel. For $B = 1$ G and $\Gamma = 2$, there is a clear hardening in the synchrotron and IC spectra produced by KN IC cooling (although a proper treatment requires EM cascading). In this photon energy range, the larger Γ is, the softer the synchrotron and IC spectra are.

For energies of photons produced by secondary pairs with energies $<\epsilon_{\rm min\ th} m_{\rm e} c^2$, the emission is produced either by synchrotron/Thomson IC cooled secondary pairs ($R \lesssim d_*$), or by secondary pairs affected already by wind advection ($R > d_*$). The spectral hardening at low energies in the synchrotron and IC emission for $R \lesssim d_*$ is produced by ionization losses. The particle pileup around $\gamma \sim 10$ impacts on the low energy radiation from $R > d_*$.

The inhomogeneity of $q(\gamma, R)$ and the sensitivity of $n(\gamma, R)$ to the cooling and transport conditions imply that the produced emission changes strongly with location in the system. Further complexities like a magnetic field with angular dependences or a strongly inhomogeneous diffusion coefficient would yield globally and locally different SEDs.

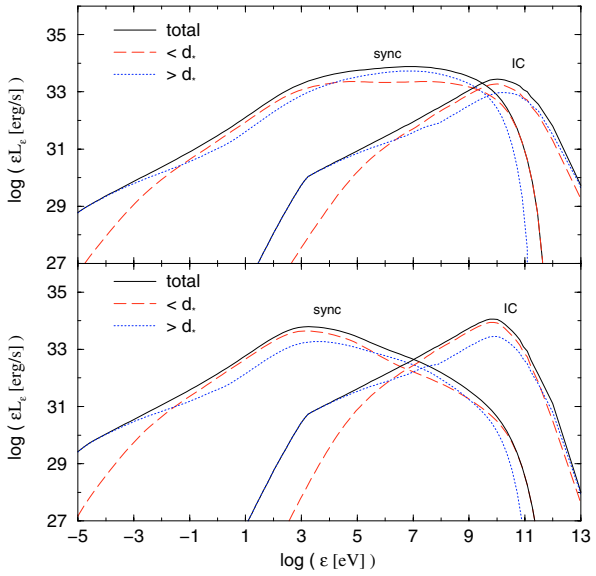

Fig. 5. *Upper panel*: computed SEDs for the synchrotron and the IC secondary pair emission. We adopt $B_0 = 100$ G and $\Gamma = 2$. The emission from the whole volume (solid line) filled by particles, and that of a region located at $R < d_* - \sim 0.1$ mas at 3 kpc- (long-dashed line) and $>d_*$ (dotted line). *Lower panel*: the same as the upper panel but for $\Gamma = 3$.

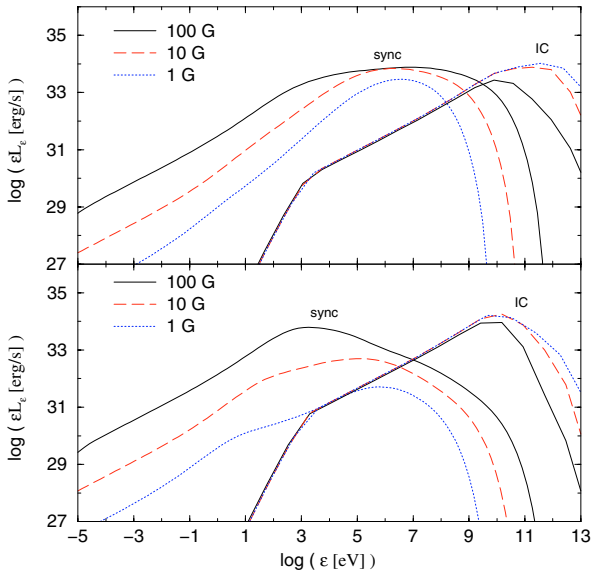

Fig. 6. *Upper panel*: computed SEDs for the synchrotron and the IC secondary pair emission. We adopt $B_0 = 1$ (dotted line), 10 (long-dashed line) and 100 G (solid line), and $\Gamma = 2$. *Lower panel*: the same as the upper panel but for $\Gamma = 3$.

3.2.1. LS 5039 and Cygnus X-1

Adopting $B_0 \sim 100$ G, our model predicts radio fluxes and X-ray luminosities of several mJy and several 10^{33} erg s^{-1}, respectively. The parameter values adopted in this work are similar to those of LS 5039 and Cygnus X-1, warranting a discussion of the results in the context of these two sources.

The obtained radio fluxes and X-ray luminosities are not far from those found in LS 5039 (e.g. Paredes et al. 2000; Bosch-Ramon et al. 2007), implying that the secondary pair contribution in this source may be comparable, if not dominant, to that of any intrinsic radio and X-ray component linked to the TeV emitter itself. Especially in the radio band, a slightly higher B-field would yield significantly larger radio fluxes due to the B^2-dependence of the synchrotron emission. The moderate X-ray luminosity in LS 5039 permits a search for such a secondary pair component. In the GeV regime, the secondary pair IC fluxes are far from those found by EGRET (Paredes et al. 2000), suggesting that the latter are due to the combination of both primary and secondary pair IC radiation.

In the case of Cygnus X-1, adopting the same $L_{\gamma\,\mathrm{inj}}$ as for LS 5039, the predicted radio flux from secondary pairs is a substantial part of the total radio flux of the source (e.g. Stirling et al. 2001). In X-rays, explained as thermal emission from accretion disk/corona-like regions, the high luminosity of Cygnus X-1 makes it impossible observationally to disentangle a possible secondary pair component.

The lack of evidence of accretion in LS 5039 (Bosch-Ramon et al. 2007, and references therein) is an important difference between this source and Cygnus X-1, which shows clear X-ray accretion features (Albert et al. 2007, and references therein). Nevertheless, as noted, e.g. by Bogovalov & Kelner (2005), the fact that in some sources the accretion disk luminosity is undetectable does not imply a lack of accretion. This may explain why LS 5039 does not show accretion signatures in its X-ray spectrum.

3.2.2. LS I +61 303

For a compact system with the properties listed in Sect. 2, only VLBI interferometers with angular resolution $\lesssim$0.1 milliarcsec would be able to resolve the radio emission. Nonetheless, within the constraints of our model, we have explored the possibility of explaining the extended radio emission of a less compact system, LS I +61 303, which presents a peculiar extended radio structure with changing morphology along the orbit (Dhawan et al. 2006). We have computed the radio emission produced at the spatial scales of the observed extended radio structures. Adopting[1] $B_0 = 100$ G, we have obtained the SEDs for the synchrotron radio emission originating in different regions: $R < 1$, >1, >2, and >3 AU. The radio and broadband (synchrotron plus IC) SEDs are presented in Fig. 7 (lower left and upper panels, respectively); the spatial distribution of the corresponding emitting particles around LS I +61 303 after an injection time of one orbital period is also shown (lower right panel).

To implement these calculations, we adopt the orbital distance corresponding to the phases when the source was detected by MAGIC (Albert et al. 2006): $\sim 6 \times 10^{12}$ cm. Γ is taken as 2.6 (Albert et al. 2006), and $L_{\gamma\,\mathrm{inj}} = 3 \times 10^{35}$ erg s^{-1}, the same as the one taken for LS 5039, enough to explain the observations. We note that LS I +61 303 is not detected by MAGIC above a few hundred GeV when outside the phase range ~0.5–0.7. Nevertheless, primary gamma rays with softer spectra may still be injecting a significant amount of secondary pairs in the system despite being barely detectable above a few hundred GeV. For the spatial distribution of particles, we followed their energy and spatial evolution individually, accounting for advection and (Bohm) diffusion in the wind using a simple Monte-Carlo simulation (Bosch-Ramon et al., in preparation). The orbital parameters of LS I +61 303 were considered (Casares et al. 2005).

From Fig. 7, it is seen that radiation flux levels of ~20 mJy (8 GHz) are reached. In this source, most of the secondary pair radio emission would appear extended, pointing in the direction opposite to the star and bending due to orbital motion, as shown

[1] The relevant parameters that determine the system properties can be found in Bosch-Ramon et al. (2006).

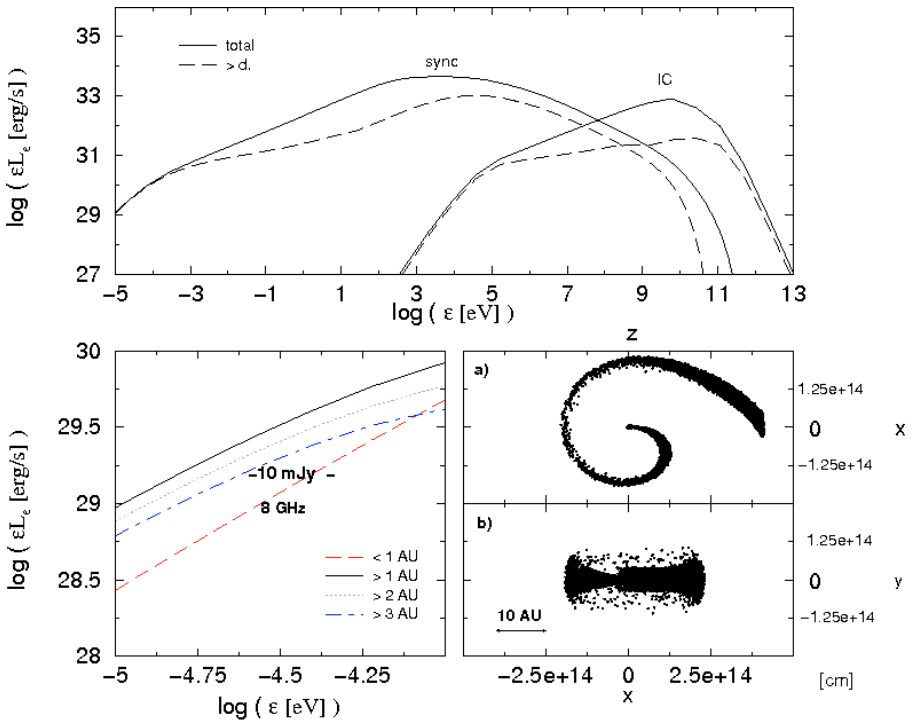

Fig. 7. *Upper panel*: computed SEDs for the synchrotron and the IC secondary pair emission produced in the whole volume (solid line) and the region beyond $>d_*$ (long dashed). We adopt $B_0 = 100$ G and $\Gamma = 2.5$. *Lower panel, left*: radio SEDs for different regions: $R < 1$ (long dashed), >1 (solid line), >2 (dotted line) and >3 AU (dot-dashed line). *Lower panel, right*: spatial distribution of the emitting particles, for the orbital plane (**a**) and a plane perpendicular to it (**b**), in the surroundings of LS I +61 303 after one orbital period. The star is centered on the origin. We note that the system size is ≈0.4 AU, and 1 AU ≈ 0.5 milliarcsec.

in the secondary pair spatial distribution in Fig. 7. This kind of behavior is similar to that found by Dhawan et al. (2006) in LS I 61 +303. These authors associated the radio morphology of this source with a particular non-accreting pulsar scenario (see Dubus 2006b), although recent hydrodynamical simulations of stellar/pulsar colliding winds predict quite different morphologies (see Romero et al. 2007; and Bogovalov et al. 2007).

The predicted X-ray luminosities are similar to those observed from this source (e.g. Sidoli et al. 2006), which, as in LS 5039, is small enough to allow the study of a secondary pair component. Despite the fact that the complexity of the X-ray emission cannot be completely explained by our model, the processes considered here may be responsible of a significant fraction of the observed X-ray emission. Like LS 5039, LS I +61 303 was also proposed to be a (variable) GeV source (Tavani et al. 1998), and the secondary pair contribution to this energy range may be significant (see also Bednarek 2006).

4. Conclusions

We conclude that the presence of a powerful VHE emitter near a massive hot star leads unavoidably to non-thermal emission in the stellar wind. The question of whether this secondary pair radiation is detectable depends on the magnetic and radiation field strength in the system.

In the scenario explored here, we predict moderately hard spectra and fluxes of several mJy for typical galactic distances, similar to the fluxes detected in some microquasars. Radio emission is produced mainly in the regions with $R > d_*$ and may be dominant over any other radio component (e.g. linked to the TeV emitter itself), and the radio morphology, flux and spectrum are strongly sensitive to the geometry and R-dependence of the magnetic field. Interestingly, the predicted radio morphology could resemble that shown by the VHE emitting X-ray binary LS I +61 303.

The fluxes of the (likely non-thermal) X-ray emission of several TeV emitting X-ray binaries (e.g. LS I +61 303, LS 5039), typically around $10^{33}-10^{34}$ erg s^{-1}, are similar to the values predicted here. It implies that the secondary pair X-ray radiation could be comparable to, or even dominate over, any intrinsic component linked to the TeV emitter itself. Because of their moderate X-ray luminosities LS 5039 and LS I +61 303 are good candidates to look for a secondary pair contribution in this energy range.

We show here that the secondary pair emission at ∼ GeV energies, if not strongly dominated by an intrinsic GeV emitter, could be revealed by GLAST. Above $\epsilon_{\rm min\ th} \sim 10$ GeV, soft primary spectra and/or moderate-to-high magnetic fields would imply low fluxes. In the latter case, significant synchrotron energy losses would suppress EM cascading.

Our calculations show that even with simple assumptions on the system geometry, primary gamma ray injected spectra, and B-field and wind structure, the resulting situation is quite complex. Thus a detailed characterization of the secondary pair non-thermal emission in a particular source is a difficult task for which stellar wind physics, primary VHE emission modeling, and high quality data are required.

Acknowledgements. The authors thank the anonymous referee for constructive comments. The authors are grateful to Andrew Taylor for a thorough reading of the manuscript. V.B.R. gratefully acknowledges support from the Alexander von Humboldt Foundation. V.B.R. acknowledges support by DGI of MEC under grant AYA2007-68034-C03-01, as well as partial support by the European Regional Development Fund (ERDF/FEDER).

Appendix A

The secondary pair injection function for a monoenergetic point-like source of target photons is determined by the following integral:

$$q(\gamma, R) = \frac{L_*}{4\pi m_e c^3 \epsilon_0} \times \int_{-1}^{1} {\rm d}\cos\theta \, \frac{(1-\cos\alpha(r))}{r^2} \int {\rm d}\epsilon \, \frac{{\rm d}N_\gamma(\epsilon)}{{\rm d}\epsilon {\rm d}t} \, {\rm e}^{-\tau} \frac{{\rm d}\sigma_{\rm p}}{{\rm d}\gamma}, \quad (3)$$

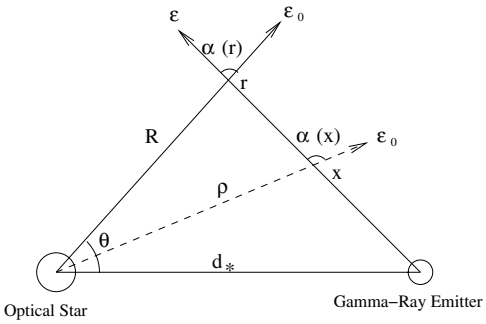

Fig. A.1. Geometry of the photon-photon interaction.

where $\mathrm{d}N_\gamma(\epsilon)/\mathrm{d}\epsilon\mathrm{d}t$ is the primary gamma ray injection spectrum per time unit, r/τ is the distance/optical depth from the gamma ray emitter to the secondary pair creation location, and $\alpha(r)$ is the interaction angle at this location. A sketch of the situation is presented in Fig. A.1. The cross-section $\mathrm{d}\sigma_\mathrm{p}/\mathrm{d}\gamma$ is given be the Eq. (15) from Böttcher & Schlickeiser (1997) and the kinematic constraints:

$$\frac{\epsilon\left(1-\sqrt{1-\frac{2}{\epsilon\epsilon_0(1-\cos\alpha(r))}}\right)}{2}<\gamma<\frac{\epsilon\left(1+\sqrt{1-\frac{2}{\epsilon\epsilon_0(1-\cos\alpha(r))}}\right)}{2}\cdot \quad (4)$$

The distance and the interaction angle are defined as the following:

$$r^2=R^2+d_*^2-2d_*R\cos\theta\,,\quad \cos\alpha(x)=\frac{\rho^2+x^2-d_*^2}{2\rho x}, \quad (5)$$

where $\rho=\sqrt{x^2+d_*^2+x(R^2-d_*^2-r^2)/r}$ is the distance from the optical star to the gamma ray absorption point. Finally, the optical depth τ is calculated with

$$\tau(r,R)=\frac{L_*}{4\pi m_\mathrm{e}c^3\epsilon_0}\int_0^r \mathrm{d}x\,\frac{(1-\cos\alpha(x))}{\rho^2}\sigma_\mathrm{p}, \quad (6)$$

where σ_p is the total pair production cross-section (see e.g. Berestetskii et al. 1982).

References

Albert, J., Aliu, E., Anderhub, H., et al. 2006, Science, 312, 1771
Albert, J., Aliu, E., Anderhub, H., et al. 2007, ApJ, 665, L51
Aharonian, F., Akhperjanian, A. G., Aye, K. M., et al. 2005a, A&A, 442, 1
Aharonian, F., Akhperjanian, A. G., Aye, K. M., et al. 2005b, Science, 309, 746
Aharonian, F. A., Anchordoqui, L. A., Khangulyan, D., & Montaruli, T. 2006a, J. Phys. Conf. Ser., 39, 408
Aharonian, F., Akhperjanian, A. G., Bazer-Bachi, A. R., et al. 2006b, A&A, 460, 743
Bednarek, W. 1997, A&A, 322, 523
Bednarek, W. 2006, MNRAS, 371, 1737
Berestetskii, V. B., Lifshitz, E. M., & Pitaevskii, L. P. 1982, Quantum Electrodynamics, Landau and Lifshitz Course of Theoretical Physics, vol. 4, 2nd Ed. (Oxford: Butterworth-Heinemann)
Bogovalov, S. V., & Kelner, S. R. 2005, ARep, 49, 57
Bogovalov, S. V., Khangulyan, D., Koldoba, A. V., Ustyugova, G. V., & Aharonian, F. 2007, MNRAS, submitted [arXiv:astro-ph/0710.1961]
Bosch-Ramon, V., Paredes, J. M., Romero, G. E., & Ribó, M. 2006, A&A, 459, L25
Bosch-Ramon, V., Motch, C., & Ribó, M., et al. 2007, A&A, 473, 545
Boettcher, M., & Schlickeiser, R. 1997, A&A, 325, 866
Böttcher, M., & Dermer, C. D. 2005, ApJ, 634, L81
Casares, J., Ribas, I., Paredes, J. M., Martí, J., & Allende Prieto, C. 2005, MNRAS, 360, 1105
Dhawan, V., Mioduszewski, A., & Rupen, M. 2006, in Proc. of the VI Microquasar Workshop, Como-2006
Donati, J. F., Babel, J., Harries, T. J., et al. 2002, MNRAS, 333, 55
Dubus, G. 2006a, A&A, 451, 9
Dubus, G. 2006b, A&A, 456, 801
Ford, L. H. 1984, MNRAS, 211, 559
Hubrig, S., Schoeller, M., & Briquet, M., et al. 2007, contribution presented at the CP/AP Workshop, Vienna-2007 [arXiv:0712.0191]
Khangulyan, D., Aharonian, F., & Bosch-Ramon, V. 2008, MNRAS, 383, 467
Maier, G. 2007, for the VERITAS collaborarion 2007, contribution to the 30th International Cosmic Ray Conference [arXiv:0709.3661]
Moskalenkon, I. V., & Karakulan S. 1994, ApJ, 92, 567
Orellana, M., Bordas, P., Bosch-Ramon, V., Romero, G. E., & Paredes, J. M. 2007, A&A, 476, 9
Paredes, J. M., Martí, J., Ribó, M., & Massi, M. 2000, Science, 288, 2340
Protheroe, R. J., & Stanev, T. 1987, ApJ, 322, 838
Puls, J., Markova, N., & Scuderi, S., et al. 2006, A&A, 454, 625
Reynoso, M. M., Christiansen, H. R., & Romero, G. E. 2008, Astrop. Phys., 28, 565
Romero, G. E., Okazaki, A. T., Orellana, M., & Owocki, S. P. 2007, A&A, 474, 15
Sidoli, L., Pellizzoni, A., & Vercellone, S., et al. 2006, A&A, 459, 901
Stirling, A. M., Spencer, R. E., & de la Force, C. J. 2001, MNRAS, 327, 1273
Tavani, M., Kniffen, D., Mattox, J. R., Paredes, J. M., & Foster, R. 1998, ApJ, 497, L89